

Characteristics of Precipitation Particles and Microphysical Processes during the 11–12 January 2020 Ice Pellet Storm in the Montréal Area, Québec, Canada

MATHIEU LACHAPPELLE^a AND JULIE M. THÉRIAULT^a

^a *Centre pour l'Étude et la Simulation du Climat à l'Échelle Régionale (ES CER), Department of Earth and Atmospheric Sciences, Université du Québec à Montréal, Montréal, Québec, Canada*

(Manuscript received 13 July 2021, in final form 24 January 2022)

ABSTRACT: Freezing rain and ice pellets are particularly difficult to forecast when solid precipitation is completely melted aloft. This study addresses this issue by investigating the processes that led to a long-duration ice pellet event in Montreal, Québec, Canada, on 11–12 January 2020. To do so, a benchmark model initialized with ERA5 data is used to show that solid precipitation was completely melted below the melting layer, which discards partial melting from the possible ice pellet formation processes. Macro photography of precipitation reveals that small columnar crystals (~200 μm) and ice pellets occurred simultaneously for more than 10 h. The estimation of ice crystal number concentration using macro photographs and laser-optical disdrometer data suggests that all supercooled drops could have refrozen by contact freezing with ice crystals. Rimed ice pellets also indicate ice supersaturation in the subfreezing layer. Given these observations, the formation of ice pellets and ice crystals was probably promoted by secondary ice production and the horizontal advection of ice crystals below the melting layer, as we illustrate using a conceptual model. Overall, these findings demonstrate how ice nucleation processes at temperatures near 0°C can drastically change the precipitation phase and the impact of a storm.

SIGNIFICANCE STATEMENT: Ice pellets are generally formed when snow particles partially melt while falling through a warm layer aloft before completely refreezing in a cold layer closer to the surface. Ice pellets can also be formed when snow particles completely melt aloft, but freezing rain is often produced in such conditions. On 11–12 January 2020, ice pellets were produced during more than 10 h in Montreal, Quebec, Canada. Macro photographs of the precipitation particles show that ice pellets occurred simultaneously with small ice crystals. Most of the ice pellets were produced while snow particles were completely melted aloft. The supercooled drops probably refroze due to collisions with the ice crystals that could have been advected by the northeasterly winds near the surface.


KEYWORDS: Cloud microphysics; Freezing precipitation; Ice crystals; Radars/radar observations; Ice particles

1. Introduction

Near 0°C winter precipitation types are both difficult to forecast and hazardous (Reeves 2016). In particular, freezing rain can cause power outages, produce dangerous conditions for automobiles and pedestrians, and significantly affect air traffic. Between 1949 and 2000, 80 freezing rain events caused \$16.3 billion (USD) worth of damage in the United States (Changnon 2003). In Canada, the 1998 Ice Storm caused \$4.6 billion (CAD) worth of damage and 35 deaths (Public Safety Canada 2012). Many aviation accidents have also been attributed to freezing rain (Isaac et al. 2001). To mitigate these hazards, aircraft must undergo de-icing processes while considering the range of precipitation types that include freezing rain, snow, ice pellets, and others (Rasmussen et al. 2000). Determining the precise type of precipitation, particularly between freezing rain and ice pellets, is challenging because they are formed in similar atmospheric conditions (e.g., Stewart et al. 2015; Ralph et al. 2005; Zerr 1997).

Freezing rain and ice pellets typically require specific atmospheric conditions. First, they can be formed through ice microphysical processes when a melting layer with temperatures (T) above 0°C sits above a subfreezing layer ($T < 0^\circ\text{C}$) that is in contact with the surface (Zerr 1997). Second, formation can also occur when a shallow cloud produces supercooled rain through the warm rain process (Raubert et al. 2000). For both processes, freezing rain eventuates when supercooled drops freeze upon impact with the surface, whereas ice pellets are already completely frozen when reaching the surface. Given the challenges of predicting freezing rain or ice pellets during winter storms, there is a need to improve our understanding of the precise mechanisms that lead to the refreezing of supercooled drops at temperatures near 0°C.

Ice pellets are generally formed when solid particles aloft partially melt before reaching the subfreezing layer. The remaining ice in the particles will initiate the refreezing into ice pellets (Penn 1957; Zerr 1997). The formation of ice pellets through the partial melting process mainly depends on the depth and maximum temperature of the melting layer aloft. The degree of saturation also impacts the melting rate (Matsuo and Sasyo 1981). Indeed, ice pellet occurrences associated with partial melting have been produced by a warm and dry melting layer (Hanesiak and Stewart 1995). Therefore, the wet-bulb temperature, which is close to the ice particle surface temperature, is

 Denotes content that is immediately available upon publication as open access.

Corresponding author: Mathieu Lachapelle, lachapelle.mathieu@courrier.uqam.ca

DOI: 10.1175/MWR-D-21-0185.1

© 2022 American Meteorological Society. For information regarding reuse of this content and general copyright information, consult the AMS Copyright Policy (www.ametsoc.org/PUBSReuseLicenses).

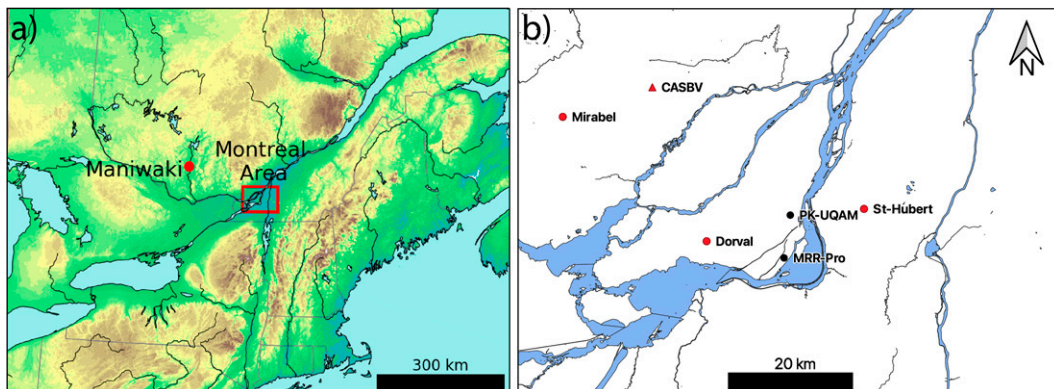


FIG. 1. (a) Topography of Southern Quebec and the northeastern United States showing the Maniwaki sounding station and the Montreal area. (b) Map of the Montreal area [red square in (a)] with PK-UQAM station, CASBV radar location, and MRR-Pro location. Mirabel, Dorval, and St-Hubert Environment and Climate Change Canada stations were also used to validate our manual observations.

usually used to characterize the temperature profile during ice pellet events (Nagumo and Fujiyoshi 2015).

Ice pellets can also be formed by the refreezing of completely melted solid precipitation (Thériault and Stewart 2010) initiated through heterogeneous freezing processes such as contact or immersion freezing (Pruppacher and Klett 1997). Hogan (1985) suggested that contact freezing with ice crystals can produce ice pellets. During the second Canadian Atlantic Storms Program (CASP II; Stewart 1991), an ice pellet event associated with a relatively warm, deep, and saturated melting layer aloft was documented. Stewart and Crawford (1995) reported ice pellets mixed with ice crystals at the surface during that storm and suggested that the drops could have refrozen through the collection of solid particles in the subfreezing layer. Pristine crystals were either observed, or detected in the subfreezing layer during other ice pellets event (Kumjian et al. 2020; Crawford and Stewart 1995; Hanesiak and Stewart 1995). Crawford and Stewart (1995) suggested that these pristine ice crystals were locally produced and originated from secondary ice produced by the Hallett–Mossop process (Mossop 1970; Hallett and Mossop 1974). Additionally, Gibson and Stewart (2007) and Gibson et al. (2009) documented ice pellet aggregates, which suggest that the presence of one ice pellet could refreeze other supercooled drops through collection.

Previous studies on ice pellets have addressed their physical characteristics (Gibson and Stewart 2007; Gibson et al. 2009), their detection using instrumentation (e.g., Kumjian et al. 2013; Nagumo et al. 2019; Tobin and Kumjian 2017; Kumjian et al. 2020), and formation mechanisms, mostly through partial melting (e.g., Stewart et al. 2015; Ralph et al. 2005; Zerr 1997). Nevertheless, little is known on the freezing processes, other than partial melting, that can lead to ice pellets. The objective of this study is to identify the microphysical and mesoscale processes that led to a long-duration ice pellet event in Montreal, Quebec, Canada (Fig. 1), during 11–12 January 2020. At PK-UQAM station, in downtown Montreal (Fig. 1b), ice pellets were reported during more than 15 h and an accumulation of 17 mm in water equivalent was measured.

ERA5 reanalysis data indicate that the melting layer was warm (up to $>5^{\circ}\text{C}$) and deep (>1.5 km) during ice pellet occurrence.

The paper is organized as follows. Section 2 gives an overview of the synoptic-scale atmospheric conditions that led to the ice pellet storm. Section 3 describes the experimental design. Section 4 presents the characteristics and timing of precipitation particles. Section 5 discusses the major microphysical processes associated with the production of ice pellets. The conclusions are stated in section 6.

2. Overview of the storm

An upper-level trough associated with a surface low pressure approaching from the south-central United States brought up to 60 mm of precipitation in rain, freezing rain, ice pellets, and snow in the Montreal area (Fig. 1a). Precipitation reached Montreal on 11–12 January 2020.

At 1200 UTC 10 January 2020, an upper-level longwave trough was located over Nevada (Fig. 2a). Between 10 and 11 January 2020, an upper-level shortwave trough separated from the longwave trough (Fig. 2b). As the upper-level shortwave moved northeastward, a low pressure system developed below the right entrance of the jet streak.

Meanwhile, lower-level southerly winds at 850 hPa and near the surface, resulted in warm air advection over the Montreal area (Figs. 2d–f). The vertical atmospheric conditions in Maniwaki, Quebec (Fig. 1a), where the closest available soundings during this event were located, are shown in Fig. 3. The ERA5 (Hersbach et al. 2020) vertical temperature profiles at Maniwaki were similar to the observations (Fig. 3). Between 1200 UTC 10 January 2020 and 1200 UTC 11 January 2020, temperatures between the surface and 800 hPa increased at both Maniwaki and Montreal.

At the PK-UQAM station, precipitation started as rain at 0800 UTC 11 January 2020. At 1800 UTC 11 January 2020, the surface temperature at PK-UQAM reached 9°C (Fig. 4a).

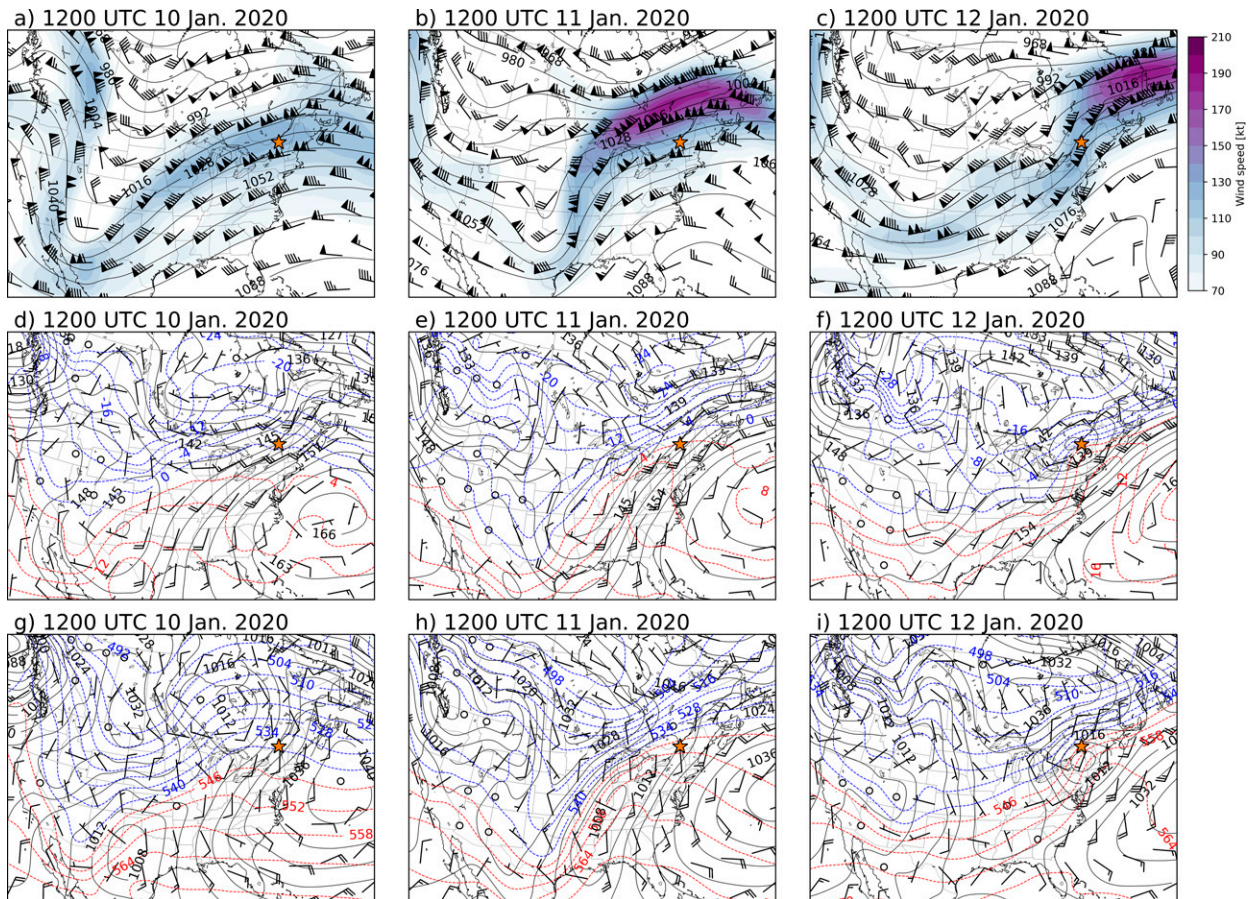


FIG. 2. (a)–(c) ERA5 reanalyses of 250-hPa wind speed and direction and 250-hPa geopotential. (d)–(f) Temperature, geopotential, and wind barbs at 850 hPa. (g)–(i) Surface pressure (solid lines) and 1000–500-hPa geopotential thickness (dashed lines). Reanalysis valid at (left) 1200 UTC 10 Jan 2020; (center) 1200 UTC 11 Jan 2020; and (right) 1200 UTC 12 Jan 2020. The star indicates Montreal location.

At around 2100 UTC 11 January 2020, the position of the low pressure system over the Great Lakes produced a horizontal pressure gradient along the St. Lawrence River Valley, leading to northeasterly winds near the surface (Carrera et al. 2009). A dual-polarization scanning radar located in Blainville, Quebec (CASBV on Fig. 1b), measured northeasterly winds up to an altitude of 1 km (Fig. 4f). Between 1800 UTC 11 January 2020 and 1000 UTC 12 January 2020, while the low pressure system was still located to the west of Montreal, surface temperatures decreased from 9.0° to −7.3°C. However, temperatures between 700 and 850 hPa remained above 0°C (Fig. 3c) due to the southerly winds at these levels, leading to ideal conditions for ice pellet development. Up to 17 mm (in water equivalent) of ice pellets was recorded between 0200 and 1600 UTC 12 January 2020. By 1200 UTC 12 January 2020, cold air advection at 700–850 hPa contributed to decrease the melting layer temperature until a transition to snow occurred between 1500 and 1600 UTC 12 January 2020. Light snow was then reported until 1800 UTC by observers at the PK-UQAM station.

3. Experimental design

a. Standard weather station

The PK-UQAM weather station is installed at an altitude of 69 m above sea level (MSL) in downtown Montreal (Fig. 1b). It is equipped with a variety of instruments to measure meteorological conditions, including precipitation amounts and types both at the surface and aloft.

The OTT Parsivel² laser-optical disdrometer (Fig. 5) measures the size and the fall speed of precipitation particles falling through the 27 mm × 180 mm sampling surface by counting the number of particles per bin in a 32 × 32 size and fall speed matrix. Values range from 0 to 25 mm and from 0 to 20 m s^{−1}. More information on the strengths and weaknesses of this instrument is provided in Battaglia et al. (2010).

Vertically pointing K-band Micro Rain Radars were used to measure the reflectivity and the Doppler velocity of the precipitation aloft. Such radars use a frequency-modulated continuous wave (Klugmann et al. 1996) to measure hydrometeor reflectivity and Doppler velocity at different heights in an atmospheric vertical column. The equivalent reflectivity

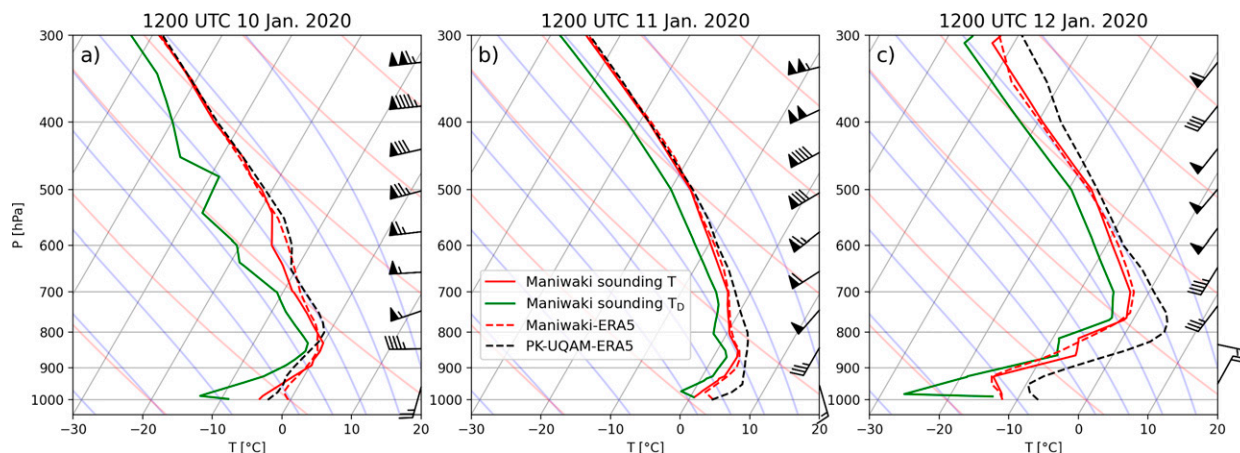


FIG. 3. Maniwaki soundings with temperature (red solid lines) and dewpoint (green solid line) and wind barbs on the right. ERA5 temperature profile at Maniwaki (dashed red lines) and at PK-UQAM station (dashed black lines) are also shown. Data are valid for (a) 1200 UTC 10 Jan, (b) 1200 UTC 11 Jan, and (c) 1200 UTC 12 Jan 2020. The soundings in Maniwaki located 100 km northwest of Montreal show good agreement with ERA5 reanalysis.

(Z_e) as well as the Doppler velocity (W) from a Micro Rain Radar 2 (MRR-2) and a Micro Rain Radar Pro (MRR-Pro) were used in this study.

The MRR-2 installed at PK-UQAM operates using 32 range gates, a vertical resolution of 200 m, and a frequency of 24.23 GHz (K-Band). There are 64 lines measured per spectrum, leading to a velocity resolution of 0.19 m s^{-1} . MRR-2 data are systematically treated using the algorithm from Maahn and Kollias (2012), which reduces noise and corrects the Doppler velocity in case of updrafts. Due to near-field effects, the algorithm does not use the first range gate. Hence, the lowest reliable range gate is at 400 m above the radar. The MRR-2 was used to analyze precipitation aloft to up to 6000 m.

For this specific event, a MRR-Pro was installed 6.6 km south of PK-UQAM station (Fig. 1b). The MRR-Pro was set to use 128 range gates with a vertical resolution of 30 m, which is a finer resolution than the MRR-2. The MRR-Pro operates at the same frequency and with the same Doppler velocity resolution as the MRR-2. The signal has less noise because of its longer acquisition time per spectrum. The two lowest range gates were not used due to near-field effect. Hence, the lowest range gate used in this study is 90 m above the radar. Due to its better resolution near the surface, the MRR-Pro was used to analyze precipitation refreezing.

b. Dual-polarization scanning radar

The dual-polarization scanning S-band radar at station CASBV in Blainville (Fig. 1), operated by Environment and Climate Change Canada (ECCC), is located 31 km to the northwest of PK-UQAM station. The dual-polarization feature is useful for assessing the representative shape and sizes of the particles, and therefore the melting and refreezing processes. To calculate the vertical profile of horizontal reflectivity (Z_H) and differential reflectivity (Z_{DR}), the quasi-vertical profile (QVP) averaging method presented in Tobin and Kumjian (2017) was used. This method consists of averaging

the data measured at different heights in a cylinder centered around the radar. The cylinder in this study had a radius of 10 km. The wind profile above the radar was also estimated using this method. To do so, radial wind speed data around the radar were fitted to a cosine function. The phase of the cosine function was associated with mean wind direction and the amplitude was associated with mean wind speed.

c. Manual observations and macro photography

Manual observations were also conducted during the ice pellet storm. Precipitation types were identified at an interval of 10 min. Precipitation types were classified as freezing rain (FZRA), freezing drizzle (FZDZ), rain (RA), drizzle (DZ), ice pellets (IP), snow (SN), and pristine ice crystals (IC). These observations were compared with observations done at ECCC stations located in Dorval, Mirabel, St-Hubert (Fig. 1b), and Trois-Rivières, which is located 120 km to the northeast of Montreal (not shown on the map).

The photography protocol follows that of Gibson and Stewart (2007). We used a Nikon Digital D3200 SLR camera, equipped with a 60-mm macro lens and a ring flash. The camera was installed on a vertical mount with a large metal base (Fig. 5). Every 10 min, solid precipitation was collected on a collection pad covered with a black velvet fabric. During collection, the pad was inserted in an opened box to limit the effect of wind on the collected particles. After collection, the pad was placed below the camera and a series of nine macro photographs of distinct area on the pad was systematically taken. Blurry photographs were manually discarded from the analysis.

Photographed particles were classified as needles (Nd), dendrites (De), columns (Co), plates (Pl), lateral plans (LP), irregular (Irr), snow pellets (SP), and ice pellets (IP) (Stark et al. 2013; Magono and Lee 1966). Following the method used in Stark et al. (2013), riming was estimated on a scale of 0 to 5. Zero represents no visible frozen droplets on the

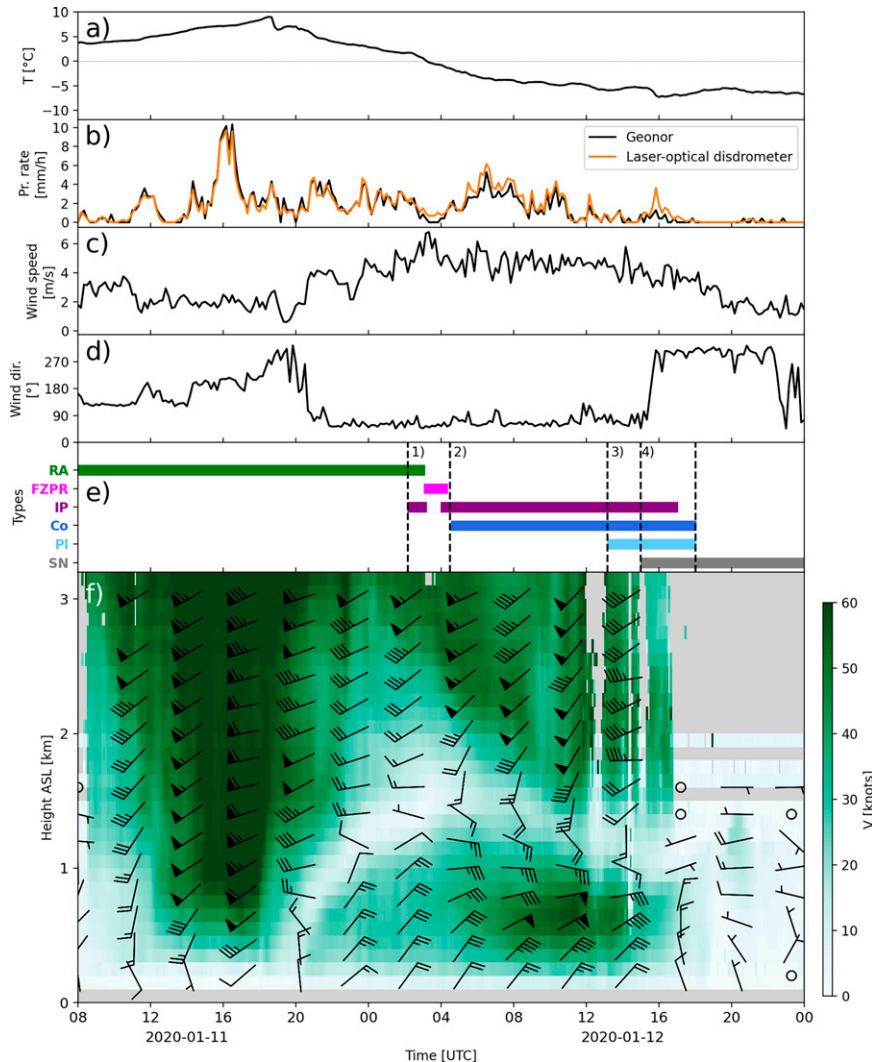


FIG. 4. Summary of PK-UQAM station measurements: (a) temperature, (b) precipitation rate measured by GEONOR and laser-optical disdrometer, (c) wind speed, and (d) wind direction. (e) The surface precipitation types observed throughout the event: rain (RA), freezing precipitation (FZPR) that includes freezing drizzle and freezing rain, ice pellets (IP), columnar crystals (Co), platelike crystals (PI), and snow (SN). Dashed vertical lines separate four intervals of solid precipitation that are characterized in section 4. (f) Quasi-vertical wind profile measured by the radar at CASBV station. Areas with no data are shown in gray.

particle, 1 means that $<25\%$ of the surface is covered, 2 means that near 50% is covered, 3 means 100% is covered, 4 represents snow habits that are barely recognizable, and 5 represents completely rimed particles. In the case of ice pellets, only levels 0–3 were used. Particles identified as ice pellets were sorted among the different categories identified by Gibson and Stewart (2007): particles with spicules, bulged, fractured, spherical, nearly spherical, and irregular particles. Other characteristics were added to the classification. For example, when possible, the presence of microbubbles in the particles was reported. However, due to the reflection of light on ice pellet surfaces, bubbles can be difficult to identify, and

many particles could not be classified according to this characteristic.

A python image processing module was used to identify single particles by applying a filter and an intensity threshold on each photograph. Due to variations in background noise between photographs, the threshold value was manually adjusted to identify all particles on every image. The major and minor axes of every particle were measured using the minimal rectangular area method. Particles with major axes under $150\ \mu\text{m}$ were automatically discarded due to low resolution. After this initial filtering process, particles that were still too blurry or too small to be identified were also



FIG. 5. (a) Camera setup used at PK-UQAM station for photography, (b) MRR-2, and (c) OTT Parsivel² laser-optical disdrometer located at PK-UQAM station.

discarded from the analysis. Although the classification of every particle was validated by a human observer, machine learning was also used to accelerate this method. Machine learning was used on the first 2000 particles of the classification process to train a convolutional neural network. The algorithm was able to discriminate between noise, ice pellets, and columnar crystals. Overall, 9633 particles including ice pellets, snow particles, and ice crystals were identified on photographs taken between 0200 UTC 12 January and 1800 UTC 12 January.

d. Reanalysis data

In the absence of sounding data available in the Montreal area, the ERA5 reanalysis data (Hersbach et al. 2020) were used to estimate the atmospheric conditions during the event. These data are produced with a horizontal resolution of 31 km and have hourly outputs. To investigate the processes that led to the occurrence of ice pellets at the surface, the vertical temperature and humidity profiles were interpolated for the coordinates of stations PK-UQAM, Maniwaki, and CASBV.

4. Timing and characteristics of observed precipitation types

The timing of precipitation amounts and types at PK-UQAM is given in Fig. 4. Rain was the only precipitation type reported between 0800 UTC 11 January 2020 and 0210 UTC 12 January 2020. The highest precipitation rates were measured during rain, at a maximum of 10 mm h^{-1} at 1600 UTC 11 January 2020. Ice pellets were first reported at 0210 UTC 12 January 2020 and occurred in combination with other types of precipitation. The combinations of precipitation types occurred over four time periods: 1) 0210–0430 UTC 12 January 2020: rain/freezing rain and ice pellet mixture, 2) 0430–1320 UTC 12 January 2020: ice pellet and columnar crystal mixture, 3) 1320–1500 UTC 12 January 2020: ice pellet and platelike/columnar crystal mixture, and 4) 1500–1800 UTC 12 January 2020: ice pellets to snow transition.

a. Freezing rain and ice pellets: 0210–0430 UTC

The first ice pellets were reported at 0210 UTC 12 January 2020. The air temperature at PK-UQAM was 1.6°C . At that time, the ratio of ice pellets over raindrops (ice/liquid ratio) was roughly estimated to vary between 10% and 50%. At 0310 UTC, the ice pellets stopped. Liquid core pellets (Thériault and Stewart 2007) were identified by cutting ice pellets and observing liquid water inside the particles (Fig. 6a). The temperature at PK-UQAM decreased to below 0°C at 0310 UTC and freezing drizzle was reported between 0310 and 0350 UTC. At 0400 UTC, ice pellets were observed again. The ice/liquid ratio steadily increased until 0420 UTC, when only ice pellets were reported. The first completely rimed ice pellet was identified at 0403 UTC (Fig. 6b) and the first ice pellets with microbubbles were identified at 0422 UTC (Fig. 6c).

b. Ice pellets and columnar crystals: 0430–1320 UTC

The first photograph that showed columnar crystals was taken at 0434 UTC, 14 min after the liquid precipitation stopped (Fig. 4). The ratio between the number of photographed ice crystals and the number of photographed ice pellets steadily increased to around 70% at 0700 UTC (Fig. 7a).

The physical characteristics of the columnar crystals evolved throughout the duration of the storm. The average major axes of the photographed columnar crystals decreased in length from $400 \mu\text{m}$ to less than $200 \mu\text{m}$ between 0434 and 0600 UTC (Fig. 7b). The size distribution of the major and minor axes of the columnar crystals before and after 0600 UTC are shown Fig. 8. The minor axes remained nearly constant from 0434 to 0600 UTC.

After 0600 UTC, the ice crystals were too small to be accurately measured by the laser-optical disdrometer, which can only reliably measure particles with minor axes larger than $250 \mu\text{m}$ (Tokay et al. 2014). To estimate the order of magnitude of the ice crystals number concentration, the number of ice pellets measured by the laser-optical disdrometer larger than the ice crystals size distribution (Fig. 8) was calculated. To do so, size bins 4–32, with $D > 374.5 \mu\text{m}$, were used. The macro photographs were then analyzed to determine the ratio between the number of ice crystals and the number of ice pellets larger than $374.5 \mu\text{m}$. The number of ice crystals falling on a horizontal area could then be calculated by multiplying the number of ice pellets measured by the laser-optical disdrometer by the ice crystals/ice pellets ratio evaluated on the photographs. Finally, the theoretical fall speed for small ice crystals (Heymsfield and Iaquinta 2000) and the size of the laser-optical disdrometer measuring area were used to evaluate the ice crystals number concentration. The resulting value is between $11\,000$ and $110\,000 \text{ m}^{-3}$, a concentration that has been measured for ice fog (Gultepe et al. 2015).

Between 0430 and 1320 UTC, hollow columns were identified on many photographs (Fig. 6f). It was difficult to evaluate the fraction of columns that were hollow because columnar crystals often appear blurry on photographs due to their small size. The presence of hollow columns indicates higher humidity in the region where ice crystals grow (Magono and Lee 1966). We observed that columns were collected by ice pellets. On macro photographs, some columns seemed to be

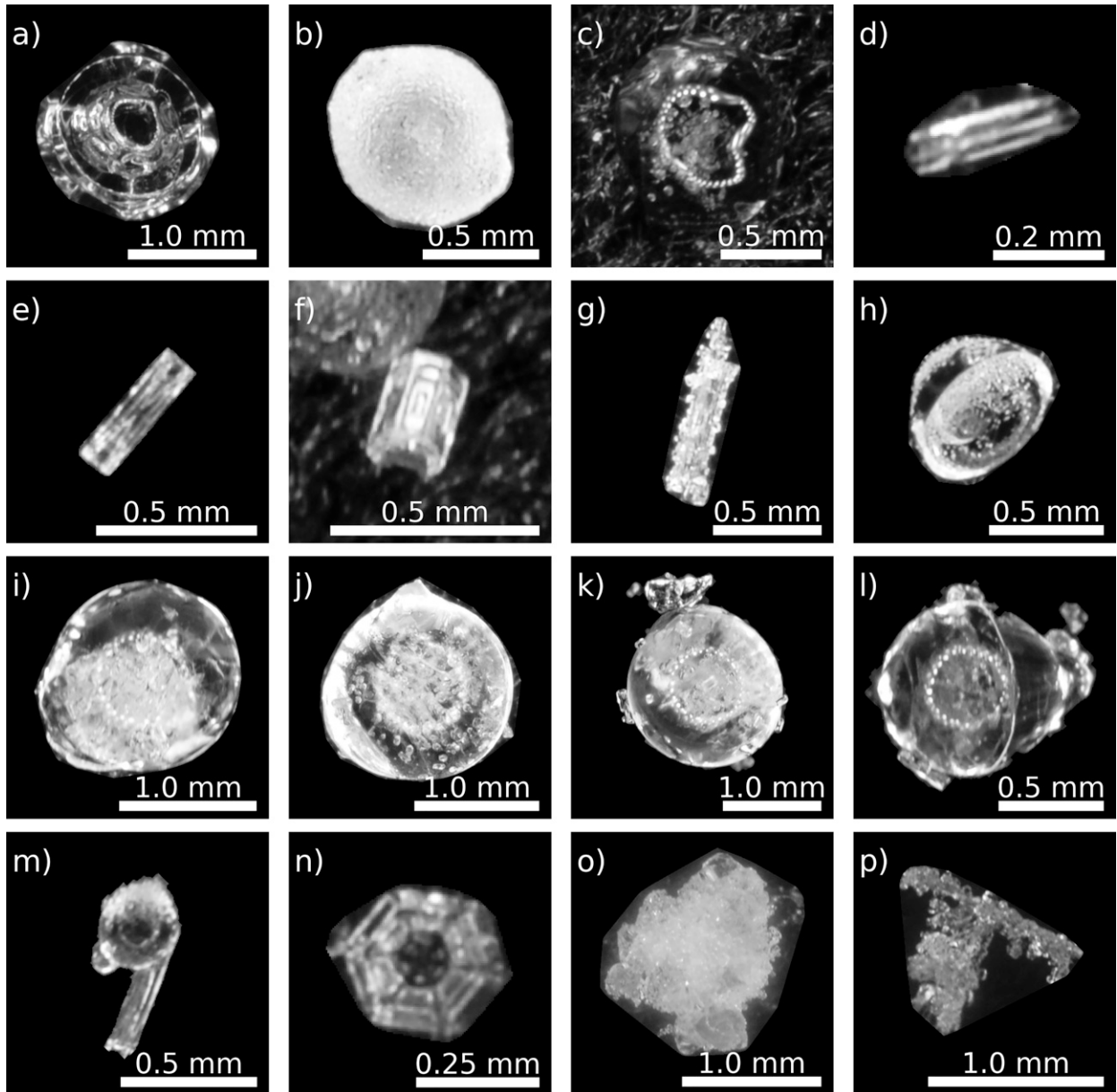


FIG. 6. Particle photographs, all of which were taken on 12 Jan. (a) Liquid core pellet at 0244 UTC. (b) First observed rimed ice pellet at 0403 UTC. (c) First ice pellet with bubbles at 0422 UTC. (d) First columnar crystal at 0501 UTC. (e) Hollow column at 0501 UTC. (f) Hollow column at 0803 UTC. (g) Rimed column at 0530 UTC. (h) Half-rimed fractured ice pellet at 0455 UTC. (i) Bulged fractured ice pellet with bubbles located near the deformation at 0814 UTC. (j) Nearly spherical ice pellet with well-distributed bubbles at 0620 UTC. (k) Spherical ice pellet with an aggregated fractured ice pellet and many columns at 0743 UTC. (l) Bulged ice pellet with aggregated columns and a visible crack at 0834 UTC. (m) Aggregated column and bulged ice pellet with preferential riming at 0501 UTC. (n) Plate at 1344 UTC. (o) Large aggregate of heavily rimed ice pellets at 1527 UTC. (p) Refrozen wet snow at 1542 UTC.

stuck on the surface of the ice pellet particle (Figs. 6k–m), and some were observed within the ice pellets (Fig. 6n). The presence of columns inside ice pellets suggests that the supercooled drop froze after coming into contact with the column. This was mostly observed for drops and columns of similar size, below 250 μm .

By 0400 UTC 12 January 2020, rimed ice pellets were observed at every 10 min observation. However, the level of

riming observed on ice pellets varied (Fig. 7c). The mean level of riming decreased between 0430 and 0730 UTC from ~ 1.5 to <1 . Some rimed columnar ice crystals were observed (Fig. 6g), and their riming levels also decreased (not shown). Some ice pellets were rimed on only a fraction of their surface (Fig. 6h), indicating the particle fell without a tumbling motion. Those particles were bulged or fractured. Even though the size of the frozen droplets varied from one particle

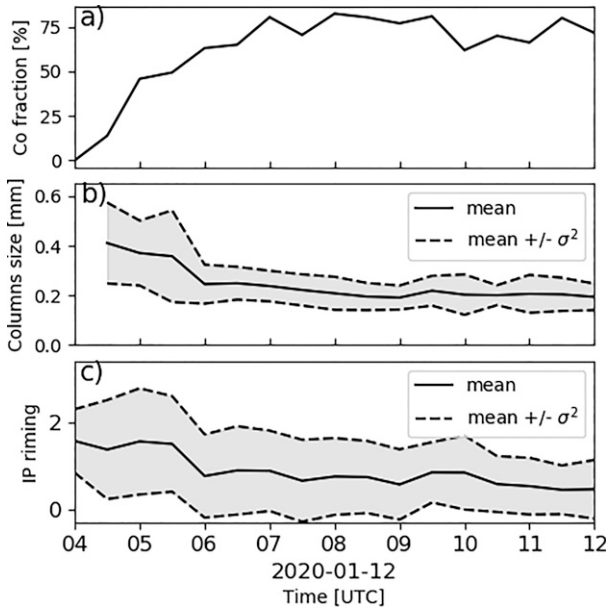


FIG. 7. Time series showing (a) the fractions of the total number of particles represented by columnar crystals (Co), (b) the averages and standard deviations (σ^2) of columnar crystals major axes, and (c) the averages and standard deviations of riming on identified ice pellets (IP) between 0400 and 1200 UTC 12 Jan 2020.

to another, some of the frozen droplets on the ice pellets are estimated to be between 10 and 50 μm .

Finally, microbubbles were clearly identified in many particles. In general, these particles were larger with bulges or

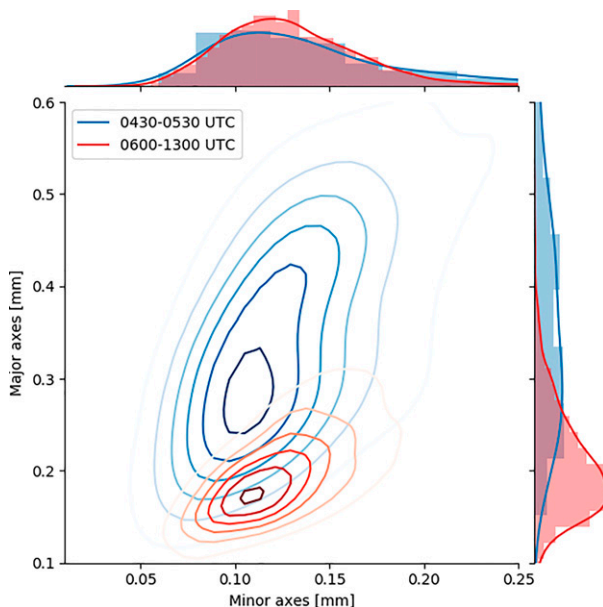


FIG. 8. Distribution of columns as a function of their minor and major axes for the columns identified between 0400 and 0530 UTC (lines in shades of blue) and for the columns identified between 0600 and 1300 UTC (lines in shades of red) 12 Jan 2020.

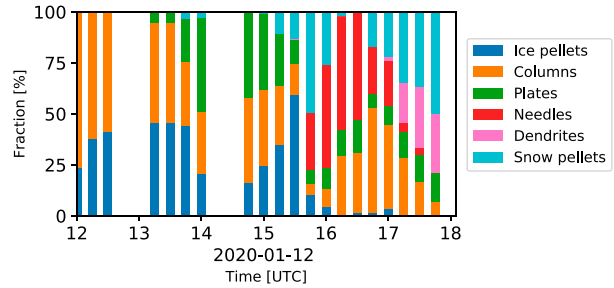


FIG. 9. Time series of the fraction of particles identified on photographs as ice pellets, columns, plates, needles, dendrites, and snow pellets between 1200 and 1800 UTC 12 Jan 2020.

other deformations. For many pellets, the bubbles were located close to a bulge or a surface deformation (Fig. 6i). For some ice pellets, the bubbles were more evenly distributed inside the particle (Fig. 6j). The size of the largest photographed bubbles is estimated to be around 50 μm .

c. Ice pellets mixed with plates and columns: 1320–1500 UTC

The first platelike crystals were photographed at 1323 UTC (Fig. 6n). The number of photographed plates increased between 1323 and 1400 UTC (Fig. 9), which shows the different ice habits observed between 1300 and 1800 UTC. At 1400 UTC, the platelike crystal population was larger than that of columnar crystals. Similar to columnar crystals, plate size distribution was centered at 200 μm and extended to a maximum of 400 μm .

d. Ice pellets to snow transition: 1500–1800 UTC

The snow transition occurred between 1500 and 1600 UTC 12 January 2020. At 1450 UTC, most of the precipitation still consisted of ice pellets, accompanied by ice crystals of columnar and platelike habits. Between 1500 and 1530 UTC, the riming on ice pellets gradually increased to nearly completely rimed. Some of these particles were aggregates of up to 10 frozen drops (Fig. 6o). Such aggregates were not observed during the other periods. This type of hydrometeor was also observed during the CASP II field experiment (Stewart and Crawford 1995). At 1540 UTC, most ice pellets were heavily rimed and refrozen wet needles appeared (Fig. 6p). Due to their large size, these needles were probably produced at a higher altitude than the smaller columnar crystals. At 1553 UTC, large snow aggregates were photographed. These aggregates mostly consisted of needles, heavily rimed snow and plates. Small rimed or unrimed ice pellets and small columns were photographed until 1710 UTC. At around 1700 UTC, dendrites started to slowly replace the needles, as the atmosphere temperature continued to decrease. The last macro photograph was taken at 1800 UTC when precipitation stopped at PK-UQAM. Intermittent snow was then reported in various locations in the Montreal area until 13 January 2020.

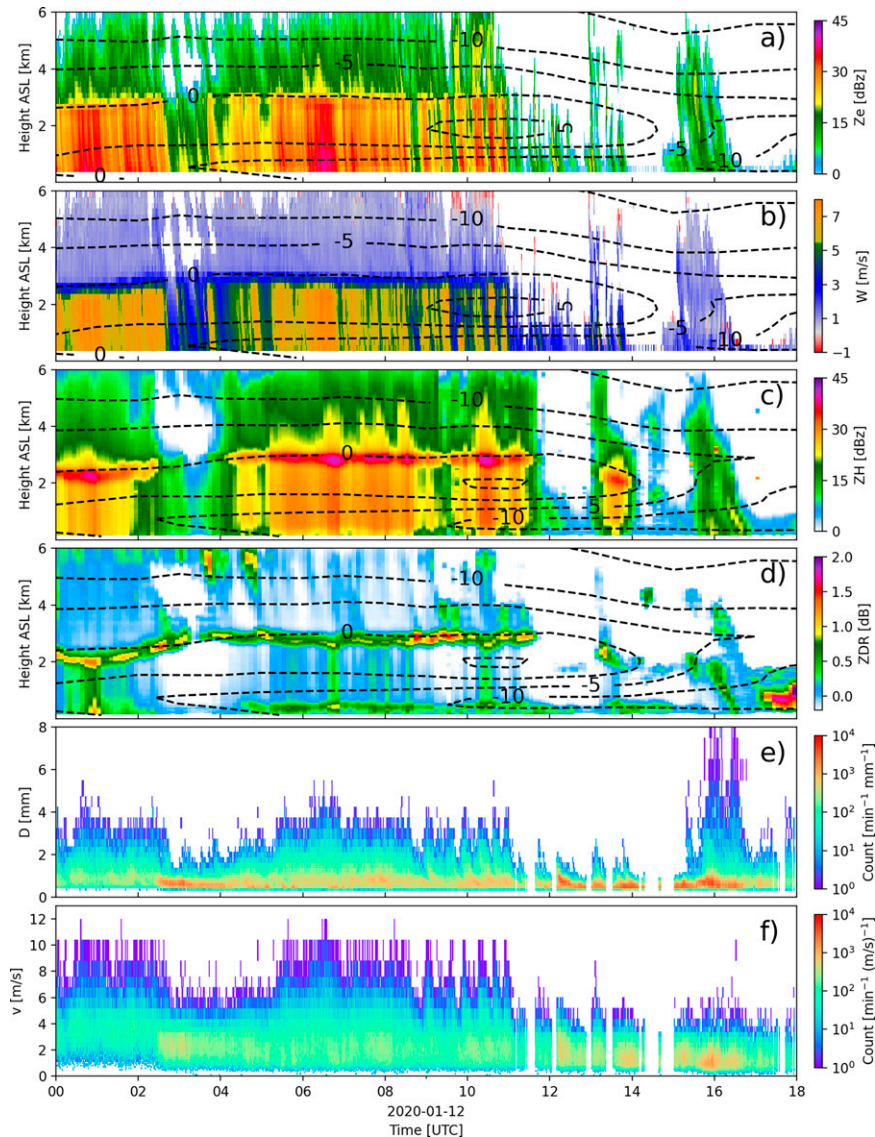


FIG. 10. Time series of ground-based remote sensing instruments on 12 Jan 2020. Station PK-UQAM MRR-2 (a) equivalent reflectivity (Z_e) and (b) Doppler velocity (W); and station CASBV dual-polarization radar measurement quasi-vertical profiles of (c) horizontal reflectivity (Z_H) and (d) differential reflectivity (Z_{DR}). The height is above sea level (ASL). The dashed lines are ERA5 isotherms interpolated for stations PK-UQAM and CASBV. Laser-optical disdrometer (e) diameter and (f) fall speed time series.

5. Microphysical processes that lead to ice pellets

a. Melting of precipitation aloft

The melting rate was evaluated using ERA5 reanalysis data. To do so, the height of the 0°C isotherm in the reanalysis data was first compared with the height of the bright band measured by the remote sensing instruments (Fig. 10). The ERA5 temperature profile was also compared with Maniwaki soundings (Fig. 3). Overall, the reanalysis data show a good agreement with the measurements.

Figure 11 shows the maximum temperature and the depth of the melting layer between 0000 and 1800 UTC 12 January. These two characteristics were calculated using the wet-bulb temperature, which is more representative of particles surface temperature (Nagumo and Fujiyoshi 2015). It shows that the transition between liquid and solid precipitation at 0210–0430 UTC was characterized by small changes in the characteristics of the melting layer (Fig. 11). At PK-UQAM, the melting layer was >1 km thick and its maximum temperature was $>1.5^\circ\text{C}$. Simulations presented

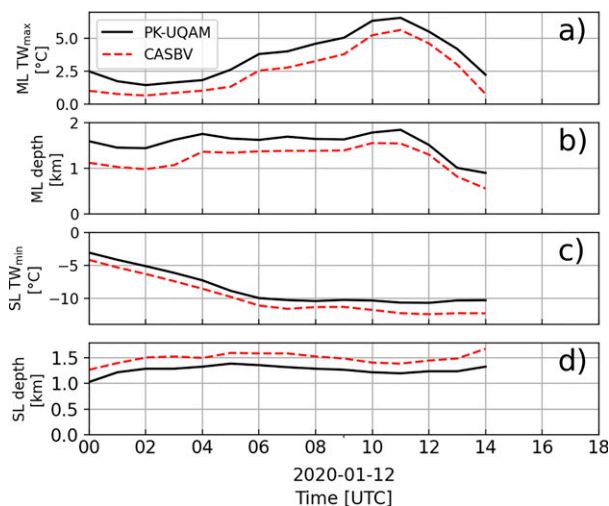


FIG. 11. Time series of the melting layer (ML) (a) maximal wet-bulb temperature (TW_{max}) and (b) depth, and subfreezing layer (SL) (c) minimal wet-bulb temperature (TW_{min}) and (d) depth at stations PK-UQAM and CASBV on 12 Jan 2020 based on ERA5 reanalysis data. The depths of the layers are calculated using the wet-bulb temperature. After 1400 UTC, the wet-bulb temperatures above Montreal and CASBV were all $<0^{\circ}\text{C}$.

in Stewart et al. (2015) and Zerr (1997) demonstrate that a melting layer with similar characteristics will completely melt 2.5-mm rimed snow particles or 20-mg dendritic snow particles (Szyrmer and Zawadzki 1999; Milbrandt and Yau 2005). During the occurrence of ice pellets, the Doppler velocity above the melting layer aloft measured by the MRR-2 remained lower than 2 m s^{-1} , indicating that the snow was not heavily rimed (e.g., Stark et al. 2013), and it therefore melted faster.

The melting rate was also computed by using a benchmark model, initialized using ERA5 temperature and humidity profiles at PK-UQAM station. A description of the benchmark model is given in appendix. In the benchmark model, ice particles melt in a two-step process, based on Cholette et al. (2019) and Rasmussen and Pruppacher (1982). During the first step, the meltwater is concentrated within the ice particles (Mitra et al. 1990), and the heat transfer between the ambient air and the ice occurs through the ventilation process. The equation used for this step was obtained from Cholette et al. (2019). During the second step, the volume of the ice-fraction is smaller than the drop formed with the melted water, and the heat transfer to the ice fraction occurs through conduction by water. Motion in the liquid fraction is neglected in our benchmark model. Rasmussen and Pruppacher (1982) mentioned that motion in the liquid fraction of the particle increases the melting rate, leading to an underestimated melting rate for our benchmark model. Nonetheless, our model suggested that large snow aggregates of up to 30 μm completely melted between 0200 and 1400 UTC 12 January.

According to ERA5 data, the wet-bulb temperature and depth of the melting layer aloft were decreasing rapidly at 1400 UTC. The wet-bulb temperature in the melting layer reached 0°C before 1500 UTC. Given this, the ice pellets

observed after 1400 UTC may have been produced through partial melting and refreezing.

In summary, given the available data and the theoretical calculations, solid precipitation was completely melted aloft during 12 h between 0200 and 1400 UTC 12 January. The small change in melting layer thickness and temperature at the start of the ice pellet occurrence suggests that the formation mechanism was dominated by a freezing process of supercooled drops rather than refreezing of partially melted solid precipitation.

b. Precipitation refreezing

Both MRRs (MRR-2 and MRR-Pro) and the S-band dual-polarization radar at CASBV were used to study the refreezing processes of supercooled drops in ice pellets. The refreezing of precipitation was detected by those instruments at $>700\text{ m}$ below the lower 0°C isotherm during most of ice pellet occurrence. This suggests that partial melting was not responsible for the refreezing of ice pellet during this period. In case of partial melting, the refreezing would have been initiated closer to the lowest 0°C isotherm.

The refreezing signatures (Kumjian et al. 2013) are visible in the time series shown in Fig. 10. A small decrease in Z_e was measured by the lowest range gate of the MRR-2, but this change in reflectivity is not associated with a change in Doppler velocity (Figs. 10a,b), as is the case for ice pellets (Yuter et al. 2008; Kumjian et al. 2020). Moreover, a decrease in Z_H near the surface at CASBV can also be seen during the same interval (Fig. 10c). Finally, a local maximum of Z_{DR} is visible near the surface between 0400 and 1500 UTC 12 January 2020 (Fig. 10d).

The local maximum of Z_{DR} is located near the elevation at which the horizontal reflectivity gradient is at its maximum, as is described in Kumjian et al. (2020) (Fig. 12). The Z_e and Z_H show a sharp decrease in intensity below 600 m. The value by which these variables decrease was relatively constant throughout the time interval. Between 90 and 500 m, Z_e decreases toward the ground by 5.5 dB on average and between 240 and 600 m, the Z_H decreases toward the ground by 4.8 dB on average. The decreases in Z_e and in Z_H are lower than the theoretical reduction of 7 dB for K-band and S-band radar that occurs if every drop freezes and remains the same size (Smith 1984; Kumjian et al. 2013; METEK 2009).

The difference between the theoretical values and the observations can be explained by a few factors. First, the density of ice is 8% lower than that of liquid water. The growth of particles caused by the change in density increased the reflectivity by 0.7 dB, compared with the theoretical values (Smith 1984). Second, ice pellet sizes can increase during refreezing due to the presence of bubbles inside, the formation of bulges and spicules, and through aggregation. These will increase the reflectivity below the refreezing level. Third, a decrease in ice pellet velocity after refreezing could also increase the particle number concentration and their radar reflectivity (Tobin and Kumjian 2021). Some studies have indeed identified that a fraction of supercooled drops can be slowed down to $1\text{--}3\text{ m s}^{-1}$ after their refreezing (Nagumo and Fujiyoshi 2015; Bukovic

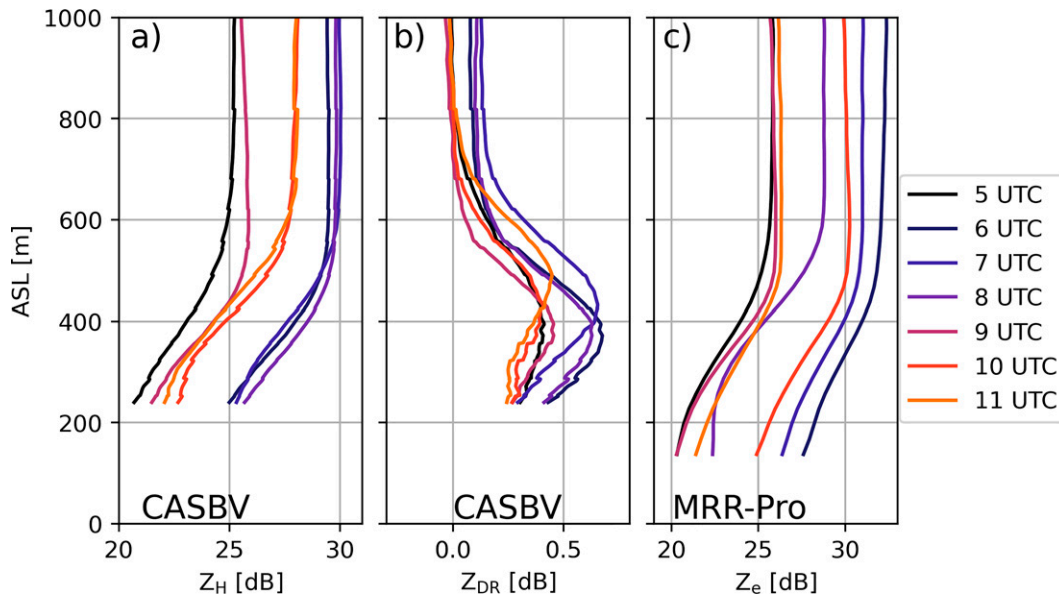


FIG. 12. Quasi-vertical profile for (a) horizontal reflectivity (Z_H) and (b) differential reflectivity (Z_{DR}) derived from dual-polarization radar measurements at CASBV and (c) reflectivity (Z_e) measured by MRR-Pro near PK-UQAM averaged at different times during ice pellet observations on 12 Jan 2020 at elevations < 1 km MSL. These three variables were averaged hourly between 0500 and 1100 UTC. During this time period, ice pellets and columnar crystals were reported at PK-UQAM station. The averages were calculated after converting reflectivity values from dB to standard units.

et al. 2017; Nagumo et al. 2019). Finally, the lowest reliable measurement from CASBV radar was at an elevation of 240 m, where precipitation might not have been completely refrozen. More analysis would be necessary to quantify the role of these different factors. In summary, the radar measurements suggest that most of the refreezing occurred below 500 m near PK-UQAM and below 600 m at CASBV.

The formation of ice pellets after 0400 UTC 12 January 2020 was associated with the freezing of completely melted liquid drops in relatively warm conditions. ERA5 reanalysis data suggest that the minimum wet-bulb temperature in the subfreezing layer was approximately -7°C by 0400 UTC 12 January 2020 (Fig. 11). This minimum temperature was located at a height of 534 m, which is very close to the refreezing signature measured by the MRR-Pro.

The different mechanisms that led to the freezing of supercooled liquid drops at temperatures near -7°C were investigated. Based on previous research, only immersion and contact freezing can occur at temperatures $> -10^{\circ}\text{C}$ (Pruppacher and Klett 1997; Phillips et al. 2009; Kanji et al. 2017). Such freezing processes can be initiated by primary ice nucleating particles (INPs) (Phillips et al. 2009; Kanji et al. 2017). A large increase in the nucleation efficiency of primary INPs has been measured between -5° and -10°C (Kanji et al. 2017). INP efficiency for immersion freezing can be measured by collecting precipitation and conducting drop-freezing assay, an experiment that measures the fraction of droplets that freeze at different temperature (Petters and Wright 2015). Previous results gathered by Petters and Wright (2015) indicate that between $5 \times 10^{-5}\%$ and 5.6%

of drops with a diameter of $1000 \mu\text{m}$ will freeze at -7°C . This suggests that only a small fraction of all supercooled drops would freeze by immersion process initiated with a primary INP. Contact freezing with an INP can also produce ice pellets. The number of ice pellets produced by contact freezing with an INP depends on the INP concentration in the atmosphere, which is evaluated between 10^{-3} and $2 \times 10^2 \text{ m}^{-3}$ at -7°C (Kanji et al. 2017). In such a concentration, the mean free path of a drop with diameter of $1000 \mu\text{m}$ is evaluated > 6 km. Given that most drops refroze in a layer thinner than 500 m, only a small fraction of drops refreezing was initiated by contact freezing with an INP.

Contact freezing can also be initiated by a collision with an ice crystal or with an ice pellet. The concentration of columnar crystals longer than $150 \mu\text{m}$ was estimated to be between $11\,000$ and $110\,000 \text{ m}^{-3}$ near the surface during the occurrence of ice pellets. Smaller, undetected ice crystals might have contributed to increase the number concentration. Given the measured size for columnar ice crystals and the resulting collision efficiency near 1 (Pruppacher and Klett 1997), a mean free path between 14 and 140 m for a drop diameter of $500 \mu\text{m}$ was computed. Drops of $1000 \mu\text{m}$ have a mean free path 4 times smaller. Given these small mean free path estimates, it is conceivable that all drops could have refrozen by contact freezing with ice crystals. Contact freezing with another ice pellet is also a possible ice pellet formation process. However, to initiate the refreezing of most ice pellets, this process requires a minimal number of ice pellets formed by another process (Barszcz et al. 2018).

To summarize, immersion and contact freezing with a primary INP and contact freezing with ice crystals or ice pellets may all have contributed to ice pellet formation during the event. In contrast with immersion or contact freezing with INPs, however, contact freezing with ice crystals could have been efficient enough to refreeze all supercooled drops.

c. Presence of ice crystals

The conditions in the subfreezing layer were analyzed to study the origin and formation process of the ice crystals. The observed ice pellets riming reveals the existence of ice-supersaturated regions located within or below the level of refreezing. Additionally, ERA5 data indicate that the temperature in the subfreezing layer was between -5° and -10°C during the period when columnar ice crystals and ice pellets were observed (Fig. 11c). This temperature is known to produce column habit growth (Magono and Lee 1966). Furthermore, the cooling of the melting layer coincided with the slow transition between column and platelike habits that were observed between 1300 and 1400 UTC 12 January 2020 (Fig. 11). Magono and Lee (1966) showed that at high supersaturation, plate growth is favored over column growth when $T < -10^{\circ}\text{C}$.

The evolution of columnar crystal characteristics over time provides additional information on the refreezing processes at the beginning of the occurrence of ice pellets. The interval between 0430 and 0600 UTC 12 January 2020 was characterized by a small number concentration of larger ice crystals (Figs. 7a,b). This interval was also characterized by a higher degree of riming for both ice pellets and ice crystals (Fig. 7c). Columnar crystals that were observed between 0430 and 0600 UTC 12 January 2020 grew larger because they had access to more moisture. Later, ice multiplication and ice crystal growth by diffusion led to an environment with more ice particles and less humidity. The decrease in riming during this time interval indicates that small droplets gradually transferred their water to ice particles through the Bergeron effect.

An activated ice nucleus is needed to initiate the formation of an ice crystal. These ice nuclei can be either primary INPs or ice particles. At -7°C , primary INP number concentration between 10^{-3} and $2 \times 10^2 \text{ m}^{-3}$ cannot explain the formation of ice crystals with number concentration between $11\,000$ and $110\,000 \text{ m}^{-3}$. Therefore, the ice nuclei responsible for ice crystals formation must be produced through secondary ice production (SIP). During this event, we suggest that two processes were responsible for SIP (Field et al. 2017). First, the refreezing of large drops produces ice splinters by droplet shattering (Keinert et al. 2020; Phillips et al. 2018). Second, the riming of ice pellets can also be an important source of SIP at temperatures between -3° and -8°C (Mossop 1970; Hallett and Mossop 1974). Saunders and Hosseini (2001) found that maximum SIP occurs when the rimer collision velocity is near 6 m s^{-1} . The laser-optical disdrometer measured many ice pellet particles with a terminal velocity near 6 m s^{-1} (Fig. 10f).

Finally, ice pellets and ice crystals could have been produced over a long-duration period by two mechanisms. First, the refreezing of a small fraction of ice pellets could have been initiated by primary INPs. This small number of ice

pellets could have produced many ice crystals, through SIP processes, and other ice pellets, through contact freezing. It is, however, difficult to evaluate if this chain reaction process could have refrozen all liquid precipitation, due to uncertainties associated with both the concentration of INPs in the atmosphere and the efficiency of SIP processes. Second, the advection of precipitation particles could also explain the presence of ice crystals, which would have been responsible for the production of ice pellets. A conceptual model showing this possible origin of ice crystals and ice pellets is presented on Fig. 13. During 11–12 January 2020 storm, snow was reported around 120 km to the northeast of Montreal. Solid precipitation particles in this region, including smaller ice crystals, could have been advected below the melting layer by the strong northeasterly winds measured by the dual-polarization radar. Near the transition between ice pellets and snow, ice pellets could have been produced either by contact freezing with solid precipitation particles or by partial melting process. Droplet shattering and rime splintering caused by the ice pellet formation would then have led to the production of ice crystals. The lower ice crystals fall speeds, ranging from a few to 30 cm s^{-1} (Heymsfield and Iaquinta 2000), would have allowed them to be advected over several kilometers before reaching the surface. For example, within 1 h, ice crystals could have been transported over 72 km by the horizontal wind measured by the dual-polarization radar ($\sim 20 \text{ m s}^{-1}$) in the subfreezing layer. Given the slow fall speed of the particles, they would have fallen by $<1080 \text{ m}$. Along the way, these ice crystals would have been scavenged by liquid precipitation, initiating the production of ice pellets and other ice crystals. This phenomenon could have expanded the ice pellet precipitation region farther south.

6. Conclusions

A long-duration ice pellet event that produced 17 mm of ice pellets in water equivalent in Montreal, Quebec, Canada, on 11–12 January 2020 was documented using reanalysis data, macro photographs, and various automated measurements of atmospheric conditions and precipitation. During a 12-h period, the observed ice pellets were associated with completely melted precipitation aloft. Little is known about the formation process of this type of ice pellet, and the analysis of this storm contributes to improve our understanding of ice pellet formation. It shows that contact freezing with ice crystals was probably responsible for ice pellet production and that the presence of ice crystals was promoted by northeasterly winds and SIP processes in the subfreezing layer.

A benchmark model was developed and initialized with ERA5 vertical temperature profiles, which revealed a deep and warm melting layer that was able to melt large snow aggregates during most of ice pellet occurrence (Zerr 1997; Stewart et al. 2015). In parallel, the CASBV dual-polarization radar, an MRR-2 and an MRR-Pro, all located in the Montreal area, indicated that most refreezing occurred at elevations below 600 m, while the lowest 0°C isotherm was located at 1300 m. In contrast with completely melted drops, partially melted particles would have started to refreeze right

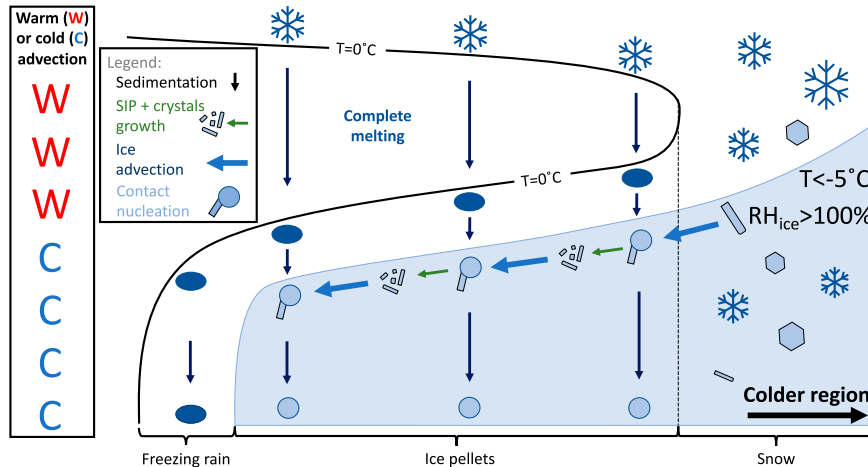


FIG. 13. Conceptual advection process that could have led to the formation of ice pellets through complete melting during the 11–12 Jan 2020 storm. The figure represents a vertical cross section with the colder region located to the right. Montreal would be located below the complete melting region, and the cross section would be aligned southwest–northeast, parallel to the low-level northeasterly winds. The surface precipitation types (shown from left to right) are freezing rain, ice pellets, and snow. The temperature advection is represented by the letters on the far left of the figure (W stands for warm advection, C stands for cold advection). The region in light blue is characterized by temperatures $< -5^{\circ}\text{C}$ with relative humidity over ice (RH_{ice}) above 100%, where columnar crystals growth is favored. On the right side of the figure, solid precipitation is slightly advected below the melting layer causing the formation of ice pellets by contact freezing. Ice pellets freezing and riming cause secondary ice production (SIP) by droplet shattering (Phillips et al. 2018) and rime splintering processes. Newly formed ice splinters grow as columnar ice crystals through vapor deposition. As these ice crystals are advected toward warmer region, more ice crystals and ice pellets are produced. Eventually, the glaciation of the subfreezing layer reaches a region where solid precipitation completely melts aloft.

below the lower 0°C isotherm. Finally, the observed transition between liquid precipitation and ice pellets occurred during small changes in the melting layer, while temperatures in the subfreezing layer were decreasing. This also suggests that partial melting was not the formation process.

ERA5 reanalysis data indicate that the minimum wet-bulb temperature in the subfreezing layer was below -7°C during ice pellet and columnar crystal precipitation. This temperature is characterized by the increase in efficiency of some primary INPs. However, immersion freezing and contact freezing with primary INPs cannot explain the refreezing of all supercooled liquid drops. In contrast, contact freezing with ice crystals could be responsible for the refreezing of all liquid precipitation. This is suggested by the high number concentration of ice crystals observed near the surface. In turn, the presence of ice crystals was probably explained by SIP that may have been caused by ice pellets refreezing and riming. The initiation of the chain reaction that induced the glaciation of the subfreezing layer was likely promoted by the advection of ice crystals from northern regions (Fig. 13).

The proposed conceptual model could also be validated through simulations and the identification of more events in which ice pellets are formed through complete melting. A climatology of ice pellet occurrences should also be carried out to evaluate the role of wind speed and direction in the subfreezing layer during such events. The role of SIP processes

such as the Hallett–Mossop process and contact freezing could also be evaluated. Overall, our research contributes to a better understanding of the processes leading to ice pellet formation when precipitation aloft becomes completely melted. This will help to improve forecasts and to differentiate ice pellets and freezing rain during winter storms.

Acknowledgments. Financial support for this study was provided by Fond de recherche du Québec–Nature et technologies, Natural Sciences and Engineering Research Council of Canada, Canada Foundation for Innovation, and Research Chair. Special thanks to Hadleigh Thompson for the development of the observation protocol. We thank Charlie Hébert-Pinard, Karel Veilleux, Aurélie Desroches-Lapointe, Félix Biron, Sébastien Marinié, Julien Chartrand, and Sara-Ann Piscopo for assistance with manual observations during winter 2019/20. Also, special thanks to Mélissa Cholette, Maud Leriche, and Frederic Fabry for constructive discussions. Finally, we want to thank the three reviewers for their constructive comments that helped to improve the manuscript.

Data availability statement. The data collected during the 11–12 January 2020 storm are available upon request to the corresponding author. The Blainville radar data are available from Environment and Climate Change Canada.

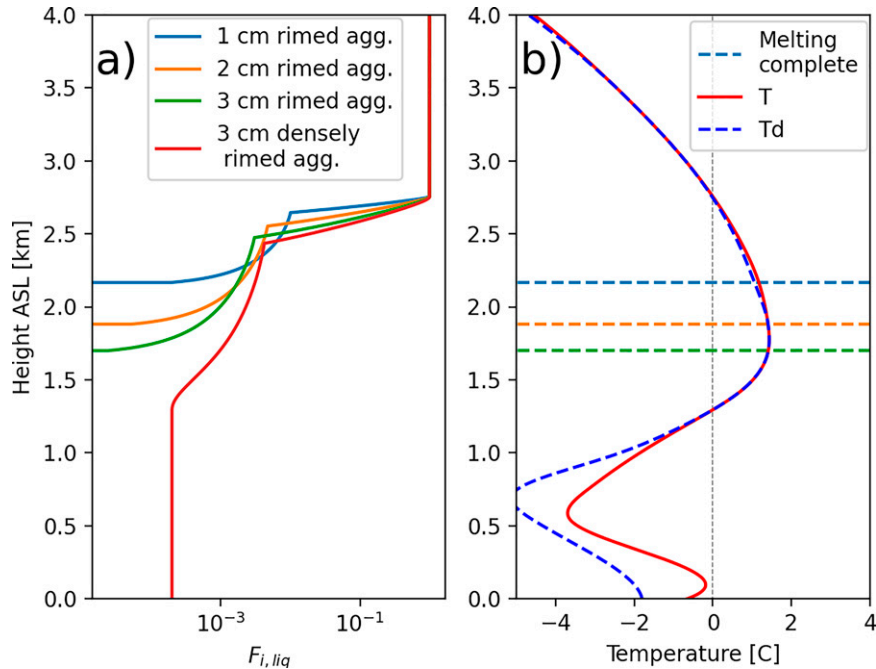


FIG. A1. (a) Liquid fraction $F_{i,liq}$ as a function of height ASL for different hydrometeor types. Only the 3-cm densely rimed aggregates do not completely melt. MRR data suggest that this type of precipitation did not form above the melting layer during 11–12 Jan 2020 storm. The x axis has a logarithmic scale. (b) ERA5 temperature and humidity profile for PK-UQAM at 0200 UTC 12 Jan. The horizontal blue, orange, and green dashed lines show the height at which the 1-, 2-, and 3-cm rimed aggregates are completely melted.

APPENDIX

Benchmark Model

To calculate the melting rate, the melting equation for single particles is used. The objective was to show that all precipitation were completely melted aloft during the ice pellet occurrence on 12 January 2020. We simulated the melting in two steps. The first step follows Cholette et al. (2019) and uses the following equation:

$$\left. \frac{dm_{ice}}{dt} \right|_{\text{melting}} = \frac{4\pi C(D, F_{i,liq})F(D, F_{i,liq})}{L_f} \times [D_v \rho_a L_e (q_v - q_{s,0}) + k_a (T - T_0)], \quad (A1)$$

where m_{ice} is the mass of ice in the particle, $F_{i,liq}$ is the liquid fraction, D is the particle diameter, $C(D, F_{i,liq})$ is the capacitance, $F(D, F_{i,liq})$ is the ventilation coefficient, ρ_a is the density of the air, q_v is the water vapor mass mixing ratio at the surface of the particle, $q_{s,0}$ is the saturated water vapor mass mixing ratio, T_0 is the temperature of the particle surface that we assume to be 0°C during melting, and T is the ambient temperature. The terms L_f and L_e are the latent heat of fusion and evaporation, D_v is the diffusivity of water vapor in the air, and k_a is the thermal conductivity of the air. The capacitance and the ventilation coefficient are parameters that govern the growing and the melting rate of ice particles.

The capacitance is calculated using a linear interpolation over $F_{i,liq}$ between the capacitance for a rain drop and the capacitance for a snow particle. The capacitance for a raindrop is equal to $0.5D$ (Pruppacher and Klett 1997), $C = 1D$ for a graupel and $C = 0.25D$ for snow aggregates (Westbrook et al. 2008).

The ventilation factor is also interpolated over $F_{i,liq}$ between the ventilation factor for a rain drop and the ventilation factor for a snow particle. For snow, we used $0.65 + 0.44 \text{Sc}^{1/3} \text{Re}^{1/2}$ and for a raindrop, we used $0.78 + 0.28 \text{Sc}^{1/3} \text{Re}^{1/2}$. Re is the Reynold number ($\text{Re} = V_i D \rho_a / \nu$) and Sc is the Schmidt number [$\text{Sc} = \nu / (\rho_a D_v)$]. Here, ν is the dynamic viscosity of the air. The term V_i is the particle fall speed that we also interpolate over $F_{i,liq}$ between the fall speed of a raindrop and the fall speed of a snow particle. The fall speed is based on Simmel et al. (2002) for raindrops and on Rasmussen et al. (1999) for snow.

The theoretical model from Rasmussen and Pruppacher (1982) and Mason (1956) for the melting of ice within a raindrop is used once the diameter of the melting particle is smaller than a drop formed from the melted snow. At this point, we consider the ice to be entirely covered with liquid water. The heat that melts the ice does not originate from ventilation but rather from conduction through liquid water. We consider ice to be contained in a sphere of radius a_i that is itself contained in a liquid drop of radius a_T . The ice sphere has the density of ice ρ_i . We neglect the motion in the liquid fraction of the particles. These two assumptions led to an overestimation of the melting time,

as shown by Rasmussen and Pruppacher (1982). The equations presented in Straka (2009) are used. The rate of melting is determined by

$$\frac{da_i}{dt} = \frac{\kappa(T_0 - T_T)a_T}{\rho_i L_f (a_T - a_i)a_i}, \quad (\text{A2})$$

where κ is the thermal conductivity of water, $T_0 = 273.15$ K is the temperature at the surface of the ice sphere, and T_T is the temperature at the surface of the liquid drop. We compute T_T with the following equation (Straka 2009):

$$\frac{4\pi(T_0 - T_T)a_T a_i}{a_T - a_i} = -4\pi a_T \kappa (T - T_T) F(D, F_{i,\text{liq}}) - 4\pi a_T L_v D_v (\rho_v - \rho_{wT}), \quad (\text{A3})$$

where T is the ambient temperature, ρ_v is the ambient density of the water vapor, and ρ_{wT} is the water vapor density at the drop surface.

Figure A1a presents the ice fraction for different types of hydrometeors as a function of height above sea level. Here, we show the humidity and temperature profile interpolated for PK-UQAM station with ERA5 reanalysis data at 0200 UTC 12 January (Fig. A1b). This time corresponds to the ice pellet occurrence with the coldest melting layer. Therefore, we can deduce that if ice completely melted at 0200 UTC, there was also complete melting during all the other ice pellet occurrences. We see on Fig. A1 that rimed aggregates of 1, 2, and 3 cm were completely melted. The two melting steps are shown in Fig. A1. The second step is characterized by a slower melting rate. Densely rimed 3-cm aggregates did not completely melt, but this type of hydrometeor is unlikely to have formed above the melting layer during the event. Indeed, above the melting layer, MRR-2 measured Doppler velocities that were slower than 2 m s^{-1} during ice pellet occurrences.

REFERENCES

- Barszcz, A., J. A. Milbrandt, and J. M. Thériault, 2018: Improving the explicit prediction of freezing rain in a kilometer-scale numerical weather prediction model. *Wea. Forecasting*, **33**, 767–782, <https://doi.org/10.1175/WAF-D-17-0136.1>.
- Battaglia, A., E. Rustemeier, A. Tokay, U. Blahak, and C. Simmer, 2010: Parsivel snow observations: A critical assessment. *J. Atmos. Oceanic Technol.*, **27**, 333–344, <https://doi.org/10.1175/2009JTECHA1332.1>.
- Bukovčić, P., D. Zrnić, and G. Zhang, 2017: Winter precipitation liquid–ice phase transitions revealed with polarimetric radar and 2DVD observations in central Oklahoma. *J. Appl. Meteor. Climatol.*, **56**, 1345–1363, <https://doi.org/10.1175/JAMC-D-16-0239.1>.
- Carrera, M. L., J. R. Gyakum, and C. A. Lin, 2009: Observational study of wind channeling within the St. Lawrence River Valley. *J. Appl. Meteor. Climatol.*, **48**, 2341–2361, <https://doi.org/10.1175/2009JAMC2061.1>.
- Changnon, S. A., 2003: Characteristics of ice storms in the United States. *J. Appl. Meteor.*, **42**, 630–639, [https://doi.org/10.1175/1520-0450\(2003\)042<0630:COISIT>2.0.CO;2](https://doi.org/10.1175/1520-0450(2003)042<0630:COISIT>2.0.CO;2).
- Cholette, M., H. Morrison, J. A. Milbrandt, and J. M. Thériault, 2019: Parameterization of the bulk liquid fraction on mixed-phase particles in the predicted particle properties (P3) scheme: Description and idealized simulations. *J. Atmos. Sci.*, **76**, 561–582, <https://doi.org/10.1175/JAS-D-18-0278.1>.
- Crawford, R. W., and R. E. Stewart, 1995: Precipitation type characteristics at the surface in winter storms. *Cold Reg. Sci. Technol.*, **23**, 215–229, [https://doi.org/10.1016/0165-232X\(94\)00014-O](https://doi.org/10.1016/0165-232X(94)00014-O).
- Field, P. R., and Coauthors, 2017: Secondary ice production: Current state of the science and recommendations for the future. *Ice Formation and Evolution in Clouds and Precipitation: Measurement and Modeling Challenges*, Meteor. Monogr., No. 58, Amer. Meteor. Soc., <https://doi.org/10.1175/AMSMONOGRAPHSD-16-0014.1>.
- Gibson, S. R., and R. E. Stewart, 2007: Observations of ice pellets during a winter storm. *Atmos. Res.*, **85**, 64–76, <https://doi.org/10.1016/j.atmosres.2006.11.004>.
- , —, and W. Henson, 2009: On the variation of ice pellet characteristics. *J. Geophys. Res.*, **114**, D09207, <https://doi.org/10.1029/2008JD011260>.
- Gulpe, I., and Coauthors, 2015: A review on ice fog measurements and modeling. *Atmos. Res.*, **151**, 2–19, <https://doi.org/10.1016/j.atmosres.2014.04.014>.
- Hallett, J., and S. Mossop, 1974: Production of secondary ice particles during the riming process. *Nature*, **249**, 26–28, <https://doi.org/10.1038/249026a0>.
- Hanesiak, J. M., and R. E. Stewart, 1995: The mesoscale and microscale structure of a severe ice pellet storm. *Mon. Wea. Rev.*, **123**, 3144–3162, [https://doi.org/10.1175/1520-0493\(1995\)123<3144:TMAMSO>2.0.CO;2](https://doi.org/10.1175/1520-0493(1995)123<3144:TMAMSO>2.0.CO;2).
- Hersbach, H., and Coauthors, 2020: The ERA5 global reanalysis. *Quart. J. Roy. Meteor. Soc.*, **146**, 1999–2049, <https://doi.org/10.1002/qj.3803>.
- Heymsfield, A. J., and J. Jaquinta, 2000: Cirrus crystal terminal velocities. *J. Atmos. Sci.*, **57**, 916–938, [https://doi.org/10.1175/1520-0469\(2000\)057<0916:CCTV>2.0.CO;2](https://doi.org/10.1175/1520-0469(2000)057<0916:CCTV>2.0.CO;2).
- Hogan, A. W., 1985: Is sleet a contact nucleation phenomenon? *Proc. 42nd Eastern Snow Conf.*, Montreal, QC, Canada, Eastern Snow Conference, 292–294.
- Isaac, G., S. Cober, J. Strapp, A. Korolev, A. Tremblay, and D. Marcotte, 2001: Recent Canadian research on aircraft in-flight icing. *Can. J. Remote Sens.*, **47**, 213–221.
- Kanji, Z. A., L. A. Ladino, H. Wex, Y. Boose, M. Burkert-Kohn, D. J. Cziczo, and M. Krämer, 2017: Overview of ice nucleating particles. *Ice Formation and Evolution in Clouds and Precipitation*, Meteor. Monogr., No. 58, 1.1–1.33, <https://doi.org/10.1175/AMSMONOGRAPHSD-16-0006.1>.
- Keinert, A., D. Spannagel, T. Leisner, and A. Kiselev, 2020: Secondary ice production upon freezing of freely falling drizzle droplets. *J. Atmos. Sci.*, **77**, 2959–2967, <https://doi.org/10.1175/JAS-D-20-0081.1>.
- Klugmann, D., K. Heinsohn, and H.-J. Kirtzel, 1996: A low cost 24 GHz Fm-Cw Doppler radar rain profiler. *Contrib. Atmos. Phys.*, **61**, 247–253.
- Kumjian, M. R., A. V. Ryzhkov, H. D. Reeves, and T. J. Schuur, 2013: A dual-polarization radar signature of hydrometeor refreezing in winter storms. *J. Appl. Meteor. Climatol.*, **52**, 2549–2566, <https://doi.org/10.1175/JAMC-D-12-0311.1>.
- , D. M. Tobin, M. Oue, and P. Kollias, 2020: Microphysical insights into ice pellet formation revealed by fully polarimetric Ka-band Doppler radar. *J. Appl. Meteor. Climatol.*, **59**, 1557–1580, <https://doi.org/10.1175/JAMC-D-20-0054.1>.

- Maahn, M., and P. Kollias, 2012: Improved micro rain radar snow measurements using Doppler spectra post-processing. *Atmos. Meas. Tech.*, **5**, 2661–2673, <https://doi.org/10.5194/amt-5-2661-2012>.
- Magono, C., and C. W. Lee, 1966: Meteorological classification of natural snow crystals. *J. Fac. Sci.*, **2**, 321–335.
- Mason, B., 1956: On the melting of hailstones. *Quart. J. Roy. Meteor. Soc.*, **82**, 209–216, <https://doi.org/10.1002/qj.49708235207>.
- Matsuo, T., and Y. Sasyo, 1981: Melting of snowflakes below freezing level in the atmosphere. *J. Meteor. Soc. Japan*, **59**, 10–25, https://doi.org/10.2151/jmsj1965.59.1_10.
- METEK, 2009: MRR physical basics, version 5.2.0.1. METEK, 20 pp., http://www.mpimet.mpg.de/fileadmin/atmosferaere/barbados/Instrumentation/MRR-physical-basics_20090707.pdf.
- Milbrandt, J. A., and M. K. Yau, 2005: A multimoment bulk microphysics parameterization. Part I: Analysis of the role of the spectral shape parameter. *J. Atmos. Sci.*, **62**, 3051–3064, <https://doi.org/10.1175/JAS3534.1>.
- Mitra, S., O. Vohl, M. Ahr, and H. Pruppacher, 1990: A wind tunnel and theoretical study of the melting behavior of atmospheric ice particles. IV: Experiment and theory for snow flakes. *J. Atmos. Sci.*, **47**, 584–591, [https://doi.org/10.1175/1520-0469\(1990\)047<0584:AWTATS>2.0.CO;2](https://doi.org/10.1175/1520-0469(1990)047<0584:AWTATS>2.0.CO;2).
- Mossop, S., 1970: Concentrations of ice crystals in clouds. *Bull. Amer. Meteor. Soc.*, **51**, 474–480, [https://doi.org/10.1175/1520-0477\(1970\)051<0474:COICIC>2.0.CO;2](https://doi.org/10.1175/1520-0477(1970)051<0474:COICIC>2.0.CO;2).
- Nagumo, N., and Y. Fujiyoshi, 2015: Microphysical properties of slow-falling and fast-falling ice pellets formed by freezing associated with evaporative cooling. *Mon. Wea. Rev.*, **143**, 4376–4392, <https://doi.org/10.1175/MWR-D-15-0054.1>.
- , A. Adachi, and H. Yamauchi, 2019: Geometrical properties of hydrometeors during the refreezing process and their effects on dual-polarized radar signals. *Mon. Wea. Rev.*, **147**, 1753–1768, <https://doi.org/10.1175/MWR-D-18-0278.1>.
- Petters, M. D., and T. P. Wright, 2015: Revisiting ice nucleation from precipitation samples. *Geophys. Res. Lett.*, **42**, 8758–8766, <https://doi.org/10.1002/2015GL065733>.
- Penn, S., 1957: The prediction of snow vs. rain. U.S. Department of Commerce, Weather Bureau, 29 pp.
- Phillips, V., and Coauthors, 2009: Potential impacts from biological aerosols on ensembles of continental clouds simulated numerically. *Biogeosciences*, **6**, 987–1014, <https://doi.org/10.5194/bg-6-987-2009>.
- Phillips, V. T., S. Patade, J. Gutierrez, and A. Bansemer, 2018: Secondary ice production by fragmentation of freezing drops: Formulation and theory. *J. Atmos. Sci.*, **75**, 3031–3070, <https://doi.org/10.1175/JAS-D-17-0190.1>.
- Public Safety Canada, 2013: Canadian Disaster Database. Accessed 15 March 2022, <https://cdd.publicsafety.gc.ca/dtpg-eng.aspx?cultureCode=en-Ca&provinces=11&eventTypes=%27SW%27&eventStartDate=%2719980101%27%2c%2719981231%27&normalizedCostYear=1&dynamic=false&eventId=277>.
- Pruppacher, H. R., and J. D. Klett, 1997: *Microphysics of Clouds and Precipitation*. Kluwer Academic, 914 pp.
- Ralph, F. M., and Coauthors, 2005: Improving short-term (0–48 h) cool-season quantitative precipitation forecasting: Recommendations from a USWRP workshop. *Bull. Amer. Meteor. Soc.*, **86**, 1619–1632, <https://doi.org/10.1175/BAMS-86-11-1619>.
- Rasmussen, R. M., and H. Pruppacher, 1982: A wind tunnel and theoretical study of the melting behavior of atmospheric ice particles. I: A wind tunnel study of frozen drops of radius < 500 μm . *J. Atmos. Sci.*, **39**, 152–158, [https://doi.org/10.1175/1520-0469\(1982\)039<0152:AWTATS>2.0.CO;2](https://doi.org/10.1175/1520-0469(1982)039<0152:AWTATS>2.0.CO;2).
- , J. Vivekanandan, J. Cole, B. Myers, and C. Masters, 1999: The estimation of snowfall rate using visibility. *J. Appl. Meteor.*, **38**, 1542–1563, [https://doi.org/10.1175/1520-0450\(1999\)038<1542:TEOSRU>2.0.CO;2](https://doi.org/10.1175/1520-0450(1999)038<1542:TEOSRU>2.0.CO;2).
- , J. Cole, R. K. Moore, and M. Kuperman, 2000: Common snowfall conditions associated with aircraft takeoff accidents. *J. Aircr.*, **37**, 110–116, <https://doi.org/10.2514/2.2568>.
- Rauber, R. M., L. S. Olthoff, M. K. Ramamurthy, and K. E. Kunkel, 2000: The relative importance of warm rain and melting processes in freezing precipitation events. *J. Appl. Meteor.*, **39**, 1185–1195, [https://doi.org/10.1175/1520-0450\(2000\)039<1185:TRLOWR>2.0.CO;2](https://doi.org/10.1175/1520-0450(2000)039<1185:TRLOWR>2.0.CO;2).
- Reeves, H. D., 2016: The uncertainty of precipitation-type observations and its effect on the validation of forecast precipitation type. *Wea. Forecasting*, **31**, 1961–1971, <https://doi.org/10.1175/WAF-D-16-0068.1>.
- Saunders, C., and A. Hosseini, 2001: A laboratory study of the effect of velocity on Hallett–Mossop ice crystal multiplication. *Atmos. Res.*, **59–60**, 3–14, [https://doi.org/10.1016/S0169-8095\(01\)00106-5](https://doi.org/10.1016/S0169-8095(01)00106-5).
- Simmel, M., T. Trautmann, and G. Tetzlaff, 2002: Numerical solution of the stochastic collection equation—Comparison of the linear discrete method with other methods. *Atmos. Res.*, **61**, 135–148, [https://doi.org/10.1016/S0169-8095\(01\)00131-4](https://doi.org/10.1016/S0169-8095(01)00131-4).
- Smith, P. L., 1984: Equivalent radar reflectivity factors for snow and ice particles. *J. Climate Appl. Meteor.*, **23**, 1258–1260, [https://doi.org/10.1175/1520-0450\(1984\)023<1258:ERRFFS>2.0.CO;2](https://doi.org/10.1175/1520-0450(1984)023<1258:ERRFFS>2.0.CO;2).
- Stark, D., B. A. Colle, and S. E. Yuter, 2013: Observed microphysical evolution for two East Coast winter storms and the associated snow bands. *Mon. Wea. Rev.*, **141**, 2037–2057, <https://doi.org/10.1175/MWR-D-12-00276.1>.
- Stewart, R. E., 1991: Canadian Atlantic Storms Program: Progress and plans of the meteorological component. *Bull. Amer. Meteor. Soc.*, **72**, 364–371, [https://doi.org/10.1175/1520-0477\(1991\)072<0364:CASPPA>2.0.CO;2](https://doi.org/10.1175/1520-0477(1991)072<0364:CASPPA>2.0.CO;2).
- , and R. Crawford, 1995: Some characteristics of the precipitation formed within winter storms over eastern Newfoundland. *Atmos. Res.*, **36**, 17–37, [https://doi.org/10.1016/0169-8095\(94\)00004-W](https://doi.org/10.1016/0169-8095(94)00004-W).
- , J. M. Thériault, and W. Henson, 2015: On the characteristics of and processes producing winter precipitation types near 0°C. *Bull. Amer. Meteor. Soc.*, **96**, 623–639, <https://doi.org/10.1175/BAMS-D-14-00032.1>.
- Straka, J. M., 2009: *Cloud and Precipitation Microphysics: Principles and Parameterizations*. Cambridge University Press, 392 pp.
- Szyrmer, W., and I. Zawadzki, 1999: Modeling of the melting layer. Part I: Dynamics and microphysics. *J. Atmos. Sci.*, **56**, 3573–3592, [https://doi.org/10.1175/1520-0469\(1999\)056<3573:MOTMLP>2.0.CO;2](https://doi.org/10.1175/1520-0469(1999)056<3573:MOTMLP>2.0.CO;2).
- Thériault, J. M., and R. E. Stewart, 2007: On the effects of vertical air velocity on winter precipitation types. *Nat. Hazards Earth Syst. Sci.*, **7**, 231–242, <https://doi.org/10.5194/nhess-7-231-2007>.
- , and —, 2010: A parameterization of the microphysical processes forming many types of winter precipitation. *J. Atmos. Sci.*, **67**, 1492–1508, <https://doi.org/10.1175/2009JAS3224.1>.
- Tobin, D. M., and M. R. Kumjian, 2017: Polarimetric radar and surface-based precipitation-type observations of ice pellet to freezing rain transitions. *Wea. Forecasting*, **32**, 2065–2082, <https://doi.org/10.1175/WAF-D-17-0054.1>.

- , and —, 2021: Microphysical and polarimetric radar modeling of hydrometeor refreezing. *J. Atmos. Sci.*, **78**, 1965–1981, <https://doi.org/10.1175/JAS-D-20-0314.1>.
- Tokay, A., D. B. Wolff, and W. A. Petersen, 2014: Evaluation of the new version of the laser-optical disdrometer, OTT Parsivel2. *J. Atmos. Oceanic Technol.*, **31**, 1276–1288, <https://doi.org/10.1175/JTECH-D-13-00174.1>.
- Westbrook, C. D., R. J. Hogan, and A. J. Illingworth, 2008: The capacitance of pristine ice crystals and aggregate snowflakes. *J. Atmos. Sci.*, **65**, 206–219, <https://doi.org/10.1175/2007JAS2315.1>.
- Yuter, S. E., D. A. Stark, M. T. Bryant, B. A. Colle, L. B. Perry, J. Blaes, J. Wolfe, and G. Peters, 2008: Forecasting and characterization of mixed precipitation events using the Micro-RainRadar. *Fifth European Conf. on Radar in Meteorology and Hydrology (ERAD08)*, Helsinki, Finland, Finnish Meteorological Institute, <http://environmentanalytics.com/pdfs/080505YuteretalERAD.pdf>.
- Zerr, R. J., 1997: Freezing rain: An observational and theoretical study. *J. Appl. Meteor.*, **36**, 1647–1661, [https://doi.org/10.1175/1520-0450\(1997\)036<1647:FRAOAT>2.0.CO;2](https://doi.org/10.1175/1520-0450(1997)036<1647:FRAOAT>2.0.CO;2).